Journal of MATERIALS RESEARCH

Article
DOI: 10.1557/jmr.2019.95

Highly responsive and selective formaldehyde sensor based on La^{3+}-doped barium stannate microtubes prepared by electrospinning

Anish Bhattacharya[1], Yufang Jiang[1], Qi Gao[1], Xiangfeng Chu[1,a)], Yongping Dong[1], Shiming Liang[2,b)], Amit K. Chakraborty[3]

[1]School of Chemistry and Chemical Engineering, Anhui University of Technology, Ma'anshan, Anhui 240003, People's Republic of China
[2]School of Materials Science and Engineering, Linyi University, Linyi, Shandong 276005, People's Republic of China
[3]Department of Physics and Centre of Excellence in Advanced Materials, National Institute of Technology, Durgapur, WB 713209, India
[a)]Address all correspondence to these authors. e-mail: maschem@sohu.com or xfchu99@ahut.edu.cn
[b)]e-mail: lsmwind@163.com

Received: 1 January 2019; accepted: 28 February 2019

La^{3+}-doped $BaSnO_3$ microtubes (La^{3+}–$BaSnO_3$) have been synthesized by electrospinning method, and the influence of La^{3+} content on the sensing properties of $BaSnO_3$ for detection of formaldehyde vapor has been investigated. The as-prepared materials have been characterized using XRD, SEM, DSC, XPS, and UV-Vis. The La^{3+}–$BaSnO_3$ sample doped with 4 wt% La exhibited a response as high as 220 to formaldehyde vapor (1000 ppm concentration) along with a very low detection limit of 0.1 ppm at 270 °C, whereas at 140 °C, it exhibited a response of 80 and detection limit of 1 ppm. In addition, the sensor showed excellent selectivity of 57 to formaldehyde at 140 °C when compared with other vapors. Further, the sensor also showed good repeatability and stability over a long period of time suggesting its strong potential as a commercial formaldehyde sensor.

Introduction

Environmental air quality is a major factor affecting human health; the presence of toxic gases in the air has been found to be responsible for serious respiratory illness [1]. Volatile organic compounds (VOCs) are ever-increasing in our environment as they find more and more applications in our day-to-day activities, and some of them, such as formaldehyde, are known to be toxic to humans. VOC detection also finds application in noninvasive medical diagnosis. Hence, the detection of VOC has become an important aspect of current day research [2, 3]. Many active materials and techniques have been developed for the detection of VOCs [4, 5, 6, 7, 8].

Semiconductor metal oxides (SMOs) have shown promising application as resistive gas sensors as the resistance of these SMOs change sharply upon adsorption of a specific analyte (VOC vapor or gas) [9]. In recent years, nanometer scale SMOs having various size and shape have gained much interest in a number of applications including gas sensors due to their size-dependent properties [10, 11, 12, 13, 14, 15, 16, 17, 18, 19, 20, 21]. Barium Stannate ($BaSnO_3$, BSO) is one such SMO which, despite having shown its potential as sensor [22, 23, 24, 25, 26, 27], has not been well explored for sensor application. For example, BSO thin films, prepared through radio frequency sputtering, as reported by Ostrick et al., showed a good response to reducing gases (isobutene, H_2, NO, CH_4, CO, etc.) at temperatures lower than 700 °C [22]. Lampe et al. reported the use of BSO thin films, deposited on an Al_2O_3 substrate through reactive sputtering, as NO sensor in the temperature range of 450–550 °C and as CO sensor in the temperature range of 600–700 °C [23, 24]. Reddy et al. investigated the effect of additives such as Pt, Pd, Rh, Ru, and Ag on the sensitivity of BSO, prepared by thermal decomposition of precursor salts followed by calcination at 1400 °C for 1 h, toward gases such as LPG, CO, and CH_4 [25]. The response time of the sensor, toward the mentioned gases, with different catalytic additives, was also studied. Lu et al. measured the electrical conductivity of Sb-doped BSO, synthesized by milling, calcination at 1100 °C, pressing, and firing in a muffle furnace at 1300–1400 °C, as a function of partial pressure of O_2 at elevated

https://doi.org/10.1557/jmr.2019.95 Published online by Cambridge University Press

© Materials Research Society 2019

temperatures in the range of 843–1000 °C [26]. Tao et al. reported the change in conductance of BSO, obtained from chemical precipitation followed by calcination at various temperatures, in the presence of air while operating in the temperature range of 200–550 °C, with conductance reaching a peak value at 290 °C; high response and good selectivity of BSO toward ethanol were also reported [27]. However, no studies have reported the formaldehyde-sensing properties of BSO, although formaldehyde detection is very important considering the associated potential hazards. Also, literature shows that doping of SMOs by various metal ions can alter the conducting properties of the SMO by creating defects [26], due to which, investigation of the influence of dopants on BSO is an interesting topic of research for sensor application.

Till now, BSO has been synthesized mostly using methods such as radio frequency sputtering [22, 23, 24], thermal decomposition [25], milling [26], chemical precipitation [27, 28], solid-state reaction [29], and thermal precipitation [30], which have their own limitations. Electrospinning is a very popular method for production of nano-to-microscale fiber mats as this technique provides many advantages in controlling the properties of the synthesized material such as high specific surface area, tunable morphology, and surface chemistry [31, 32]. In this technique, the flow of a polymer solution is controlled by a syringe pump under high voltage maintained between the needle and metal collector surface acting as electrodes. Properties of the solution, the electrical parameters of the setup, and ambient conditions significantly affect the electrospinning process and properties of the synthesized material [33]. As a consequence, it has gained a lot of attention in recent times, as is evident from the increase in patents and publication in areas such as energy engineering, tissue engineering, life sciences, and sensors [34, 35]. However, there are no reports on the synthesis of BSO tubes using electrospinning, and hence, considering the necessity of large surface area for good sensing response of the sensor material, it is expected that electrospinning-synthesized BSO tubes could exhibit excellent sensing properties to VOCs, including formaldehyde. Further, since the electrical conductivity of semiconductors can be significantly altered by introducing dopants, doping BSO tubes with appropriate dopants is likely to improve the sensing response of BSO sensors.

In view of the above, here we report the synthesis of BSO and La^{3+}-doped BSO microtubes through electrospinning for application in formaldehyde sensor. The choice of La as dopant was based on its widespread use in recent literature as a dopant in SMOs for a number of applications [36]. The as-prepared LBSO samples of different dopant concentration were tested for sensing of formaldehyde vapor within a large temperature window to identify the optimum operating temperature as well as the optimum dopant concentration. The optimally doped LBSO sample (4 wt% La) was further characterized by a number of techniques for structural, optical, and chemical information which were correlated to its good sensing properties.

Results and discussion

The TG-DSC curves of precursors used for sample preparation have been illustrated in Fig. 1(a). As is evident from Fig. 1(a), the precursors go through several steps of weight loss. The first weight loss occurs between room temperature (25 °C) and 85 °C, accompanied by an endothermic peak which originates from the removal of the adsorbed impurities. The second weight loss occurs between 85 and 200 °C, accompanied by an exothermic peak corresponding to the removal of the structural water from the salts. The third weight loss occurs during heating from 200 to 400 °C, with a weight loss of approximately 30%, accompanied by two exothermic peaks. Within this temperature range, the first peak at 288 °C indicates the decomposition and subsequent vaporization of DMF and PVP, whereas the second peak at 327 °C results from the decomposition of the metallic salts leading to the formation of BaO, SnO_2, and La_2O_3 as well as loss of NO_2 and HCl gases. The sample then goes through a phase transition in the temperature range of 400–500 °C, resulting in the formation of $BaSnO_3$ [27, 37, 38]. Another phase transition occurs in the

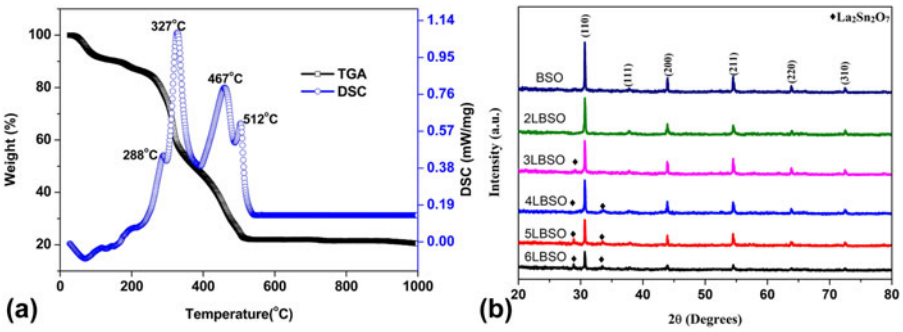


Figure 1: (a) TG-DSC curves of 4LBSO and (b) X-ray diffractograms of BSO and various LBSO samples; the peaks representing planes of $La_2Sn_2O_7$ crystals are marked separately.

https://doi.org/10.1557/jmr.2019.95 Published online by Cambridge University Press

© Materials Research Society 2019

temperature range of 500–550 °C, marked by an exothermic peak resulting from the formation of $La_2Sn_2O_7$. The reactions involved in the synthesis process are shown as follows:

$$2Ba(NO_3)_2 \xrightarrow{\Delta} 2BaO + 4NO_2(\uparrow) + O_2(\uparrow) \quad , \qquad (1)$$

$$SnCl_4 \cdot 5H_2O \xrightarrow{\Delta} SnO_2 + 4HCl(\uparrow) + 3H_2O \quad , \qquad (2)$$

$$La(NO_3)_3 \cdot 6H_2O \xrightarrow{\Delta} La_2O_3 + NO_2(\uparrow) + H_2O \quad , \qquad (3)$$

$$BaO + SnO_2 \xrightarrow{\Delta} BaSnO_3 \quad , \qquad (4)$$

$$La_2O_3 + 2SnO_2 \xrightarrow{\Delta} La_2Sn_2O_7 \quad . \qquad (5)$$

Figure 1(b) depicts the powder X-ray diffraction (XRD) patterns of BSO and LBSO samples in which peaks corresponding to planes (110), (111), (200), (211), (220), and (310) of cubic $BaSnO_3$ (PDF#15-0780) phase can be identified at 2θ values 30.69°, 37.83°, 43.96°, 54.56°, 63.91°, and 72.56°, respectively, in all the samples. Two additional weak peaks are also observed for LBSO samples containing more than 2 wt% La^{3+} at 2θ values of 28.97 and 33.54 which correspond to (222) and (400) planes of cubic $La_2Sn_2O_7$ phase (PDF#13-0082), respectively.

The crystallite size of the samples was calculated using the Debye–Scherrer formula. Addition of La^{3+} sharply reduced the crystallite size by a significant amount with the minimum size of 48.18 nm at 4 wt%, doping above which the size of the crystallites started to increase again. The crystallite size of the BSO was found to be similar to the previously reported crystallite size of 60.63 nm [39].

Rendered in Figs. 2(a)–2(d) are Field Emission Scanning Electron Microscope (FESEM) micrographs of 4LBSO nanoparticles at different magnifications. As is evident from the images, the LBSO microtubes were made out of smaller LBSO nanoparticle. Analysis of these images shows that, on average, the microtubes had a diameter of 280 nm and an average length of 2.5 μm, approximately. The average nanoparticle size was found to be ~55 nm which agrees well with the crystallite size (~48 nm) calculated from the XRD patterns.

Figure 3(a) shows the UV-Vis diffused spectra of 4LBSO sample. A Tauc plot was drawn using the raw data of Fig. 3(a), as shown in Fig. 3(b). Subsequently, the electronic band gap of 4LBSO was found to be 3.61 eV. Figure 3(c) depicts the Tauc plots as obtained by converting the UV-Vis diffused spectra of each of the samples. It is evident from the intercepts with the *x*-axis that the band gap energy of the samples, as shown in Fig. 3 (d), decreased initially with the addition of La^{3+}, reaching a minimum value of 3.61 eV at 4 wt% La^{3+}. Thereafter, the band gap energy was found to increase with the addition of La^{3+}.

Figure 4(a) illustrates the X-ray Photoelectron Spectroscopy (XPS) survey spectrum of 4LBSO sample confirming the presence of Ba, Sn, La, and O in the sample. In addition, the spectrum also confirms the cleanliness of the sample as no impurity peaks apart from those due to C (adventitious) could be observed. All data were calibrated with respect to the position of the C 1*s* peak at 285 eV, observed due to the presence of adventitious Carbon, in accordance with the literature [40, 41].

Figures 4(b)–4(e) plot the spectra obtained from Sn 3*d*, Ba 3*d*, O 1*s*, and La 3*d* core levels, respectively. The Sn $3d_{5/2}$ and

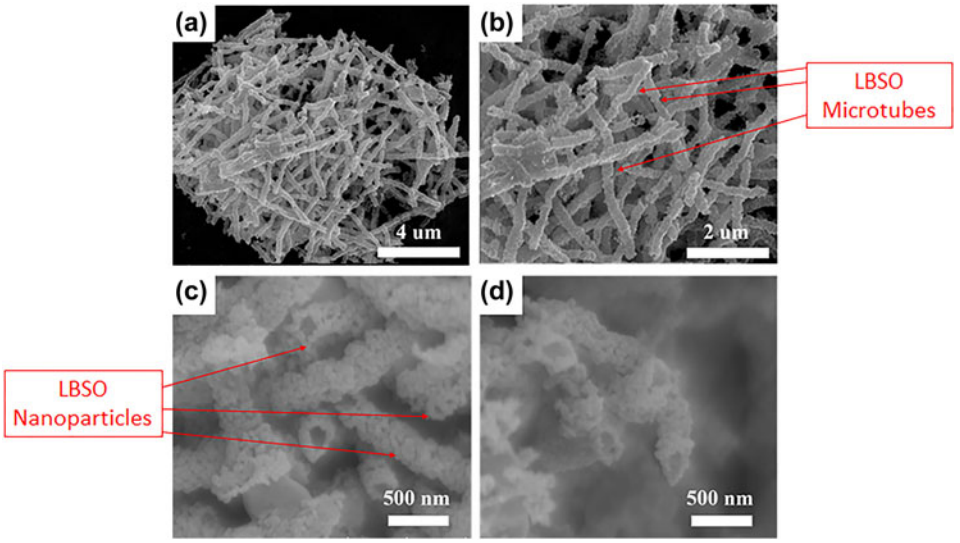


Figure 2: (a)–(d) SEM micrographs of 4LBSO microtubes made from 4LBSO nanoparticles at various magnifications.

https://doi.org/10.1557/jmr.2019.95 Published online by Cambridge University Press

© Materials Research Society 2019

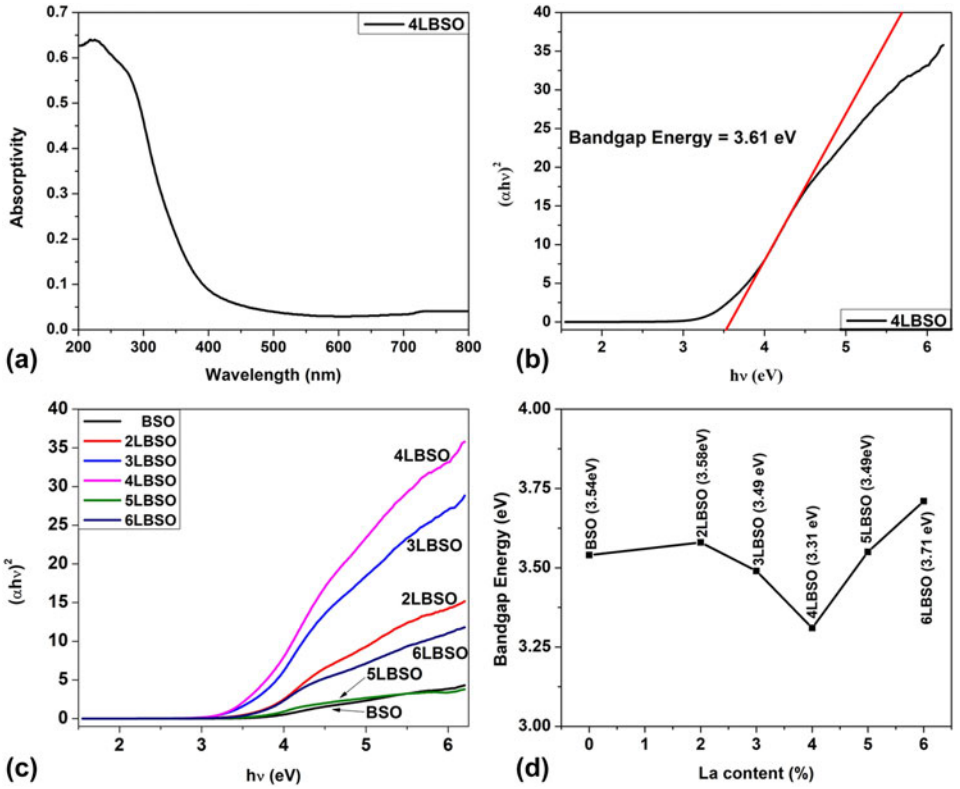


Figure 3: (a) UV-Vis diffused spectra of 4LBSO, (b) tauc plot obtained from UV-Vis diffused spectra of 4LBSO along with slope showing intercept at the *x*-axis, (c) tauc plots obtained from the UV-Vis diffused spectra of BSO samples with varying La^{3+} content, and (d) comparison of the values of energy band gap as obtained from Tauc plot for all BSO samples as a function of La^{3+} dopant concentration.

Sn $3d_{3/2}$ peaks, shown in Fig. 4(b), were observed at 486.3 eV and 494.7 eV, respectively, with a peak separation of 8.4 eV in good agreement with literature suggesting Sn^{4+} states [42]. The Ba $3d_{5/2}$ and Ba $3d_{3/2}$ peaks, shown in Fig. 4(c), were observed at binding energies of 780.4 eV and 795.7 eV, respectively, confirming the presence of Ba^{2+} oxidation state [42]. The asymmetric peak in Fig. 4(d), can be deconvoluted into three peaks centered at 532.2, 531.4, and 530.2 eV, confirming the presence of chemisorbed oxygen species on the surface of BSO (O^{2-}), oxygen vacancies (O^{-}), and lattice oxygen species (O_2^{-}), respectively [43, 44]. The La 3*d* spectrum, shown in Fig. 4(e), was fitted such that the two components representing La $3d_{5/2}$ are located at 835.2 and 838.86 eV, whereas the components due to La $3d_{3/2}$ are located at 852.46 and 855.84 eV, thus, confirming the presence of La^{3+} ions in the sample. The two components of La $3d_{5/2}$ and La $3d_{3/2}$ result from spin–orbit interaction occurring separately in each spin–orbit component [45].

Figure 5(a) shows the N_2 adsorption–desorption isotherm plots obtained by the Brunauer–Emmet–Teller (BET) method for 4LBSO. The specific surface area of the sample was calculated to be approximately 8.6 m^2/gm, whereas a pore size diameter of about 14.5 nm for 4LBSO was obtained from analysis of Fig. 5(b).

Analysis of gas-sensing response

The change in the resistance of the LBSO sensor caused by its exposure to formaldehyde was used to measure the sensor response using the following equation.

$$S = \frac{R_a}{R_g} \quad , \tag{6}$$

where R_a is the electrical resistance of the gas sensor in air and R_g is the electrical resistance of gas sensor in the presence of the gas.

Figure 6(a) shows the response of all the samples to 1000 ppm concentration of formaldehyde at different temperatures. It can be seen that, above a threshold temperature of 75 °C, the formaldehyde-sensing response of 3LBSO, 4LBSO, and 5LBSO increased with increasing the temperature. Interestingly, the 2LBSO sample showed sensing response toward formaldehyde only after the temperature was raised above 210 °C. All samples showed their best response toward formaldehyde at an operating temperature of 270 °C above which it started to decrease, and 4LBSO sample showed the highest response (220) compared to all other samples tested.

The response of 4LBSO sample to 1000 ppm of various VOCs as a function of temperatures has been illustrated in

https://doi.org/10.1557/jmr.2019.95 Published online by Cambridge University Press

© Materials Research Society 2019

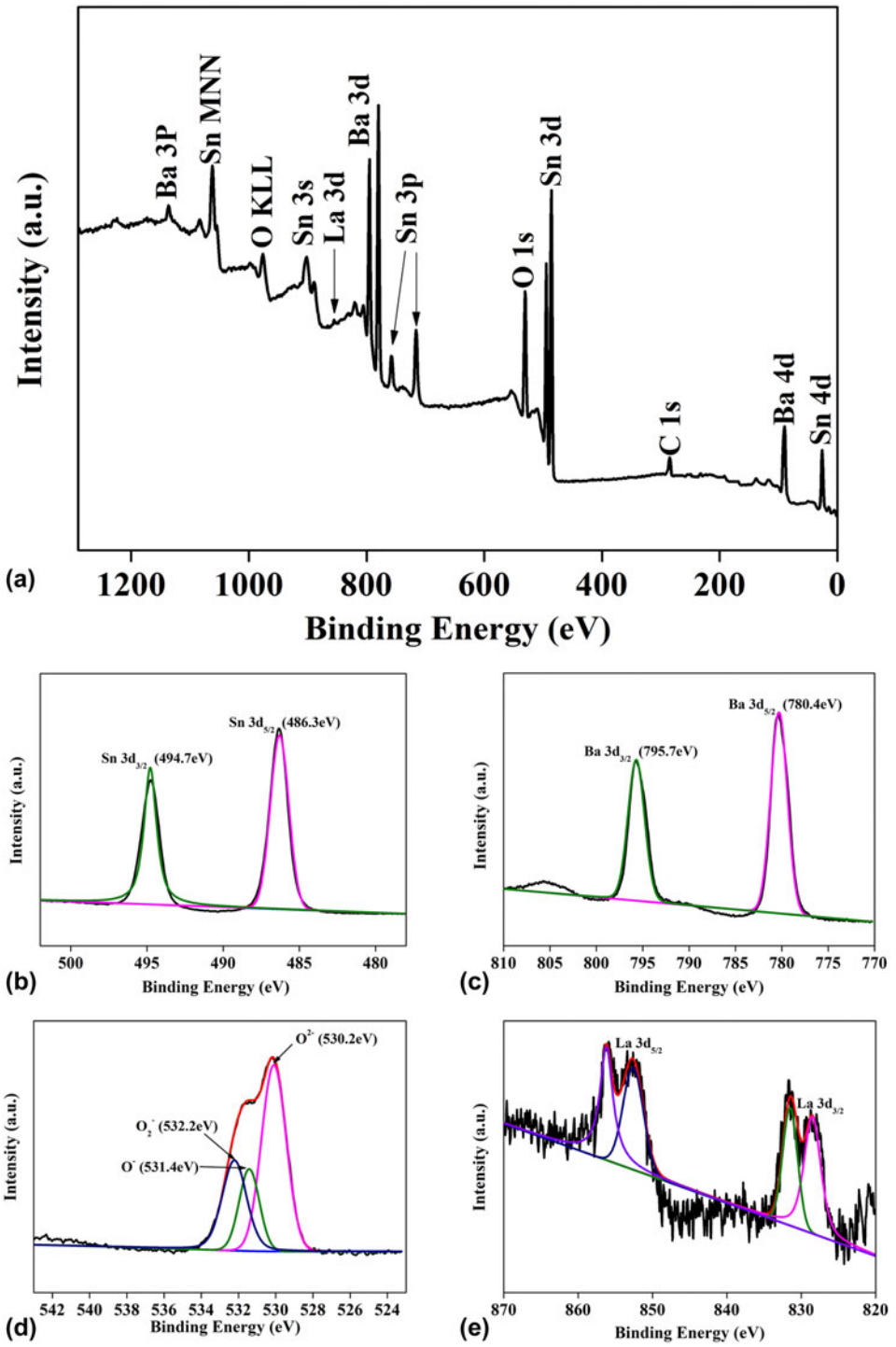


Figure 4: XPS spectra of 4LBSO sample: (a) survey, (b) Sn 3*d*, (c) Ba 3*d*, (d) O 1*s*, and (e) La 3*d* spectra, respectively.

Fig. 6(b). It can be observed that 4LBSO showed some response to ammonia, acetaldehyde, acetic acid, and ethanol at room temperature which decreased rapidly as the temperature was increased and disappeared at 50 °C above which it increased again. Among all the VOCs tested, the best response was obtained at 270 °C to formaldehyde.

The selectivity of the sample, G, is defined as follows:

$$G = \frac{S_1}{S_2} \quad , \tag{7}$$

where S_1 is the response of the sample to formaldehyde at a particular temperature and S_2 is the significant response shown

https://doi.org/10.1557/jmr.2019.95 Published online by Cambridge University Press

© Materials Research Society 2019

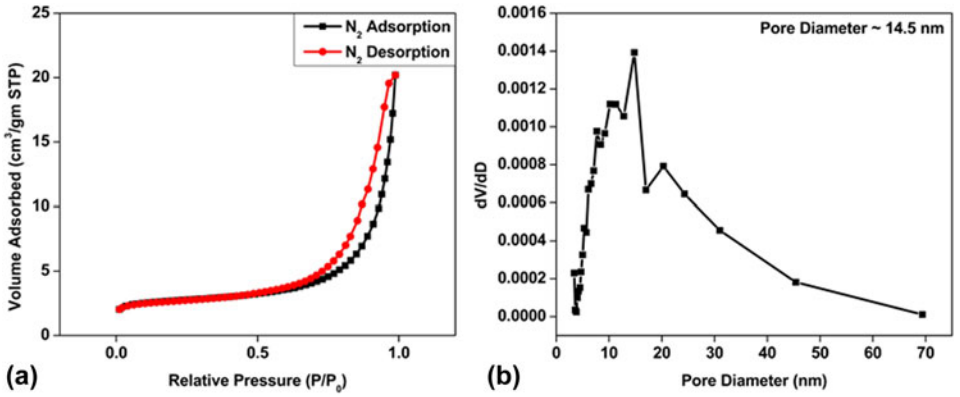


Figure 5: (a) N_2 adsorption–desorption isotherm plot for 4LBSO and (b) corresponding pore size distribution.

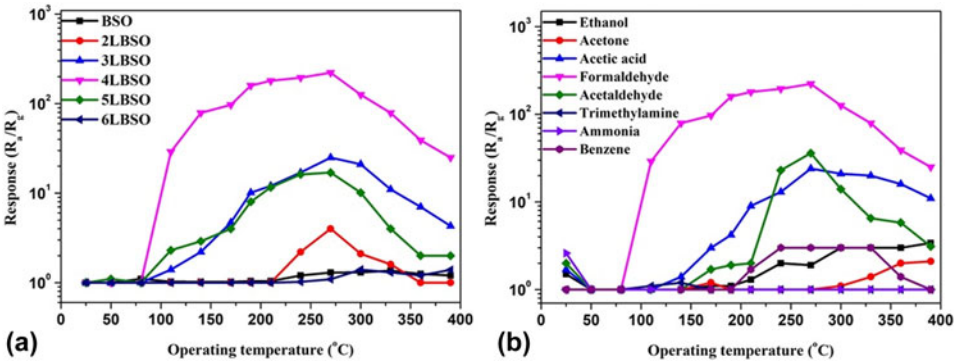


Figure 6: (a) Influence of La content on the sensing response of the various BSO and LBSO samples when exposed to 1000 ppm concentration of formaldehyde as a function of temperature, and (b) response of 4LBSO to various VOCs at a concentration of 1000 ppm.

to other gas at the same temperature. Using the data obtained from Fig. 6(b) in Eq. (7), we obtained $G = 57.14$ at 140 °C which is much higher than its value (6.29) obtained at 270 °C, thus confirming that the sample's best selectivity is at 140 °C.

Figures 7(a) and 7(b) depict the response time plot for the 4LBSO sensor to different concentrations of formaldehyde at operating temperatures of 270 °C and 140 °C, respectively. Further, the 4LBSO sample showed a very low detection limit of 0.1 ppm, with a response of 1.33 at 270 °C and at 140 °C, it increased to 1 ppm with a response of 1.6. Figure 7(c) shows that the sensor response is highly reproducible at 270 °C even after five cycles, whereas Fig. 7(d) shows that the sensor response gradually rises as the concentration of formaldehyde is increased.

The stability of the sample has been shown in Fig. 8. The response of the sample remained stable in the range of 215–225 for 3 days following which the response declined to approximately half of the original value on the 4th day. The sample then maintained the modified response for a prolonged period of 31 days.

Formaldehyde-sensing mechanism of LBSO

The sensing mechanism in metal oxide gas sensors is generally explained by the ionosorption of oxygen species on the SMO surface when operating in ambient air. In the temperature range between 100 and 200 °C, oxygen ionosorbs in a molecular (O_2^-) form and at higher temperatures the atomic form (O^-) may be responsible since O_2^- has a lower activation energy than that of (O^-) [46, 47, 48, 49]. BSO being a wide band gap n-type semiconductor and due to its microfiber-like morphology combined with defects produced by La doping, favors the adsorption of oxygen species on its surface and subsequent adsorption of test gases. The adsorption of oxygen species on the surface of the LBSO based sensor, during heating, can be described by the following equation:

$$O_2(\text{ad}) \leftrightarrow O_2^-(\text{ad}) \leftrightarrow 2O^-(\text{ad}) \leftrightarrow 2O^{2-}(\text{ad}) \quad . \qquad (8)$$

As the adsorbed species capture electrons from the SMO, they bring about an increase in the resistance of the SMO caused by the enlargement of the space-charge region.

As the surface of the SMO is further exposed to an analyte gas, the analyte molecules adsorb on its surface which soon interacts with the preadsorbed O^{2-} species. The following reaction, as reported by Wu et al. [50], shows a possible exchange scenario that might occur on the surface of LBSO when it is exposed to formaldehyde:

https://doi.org/10.1557/jmr.2019.95 Published online by Cambridge University Press

© Materials Research Society 2019

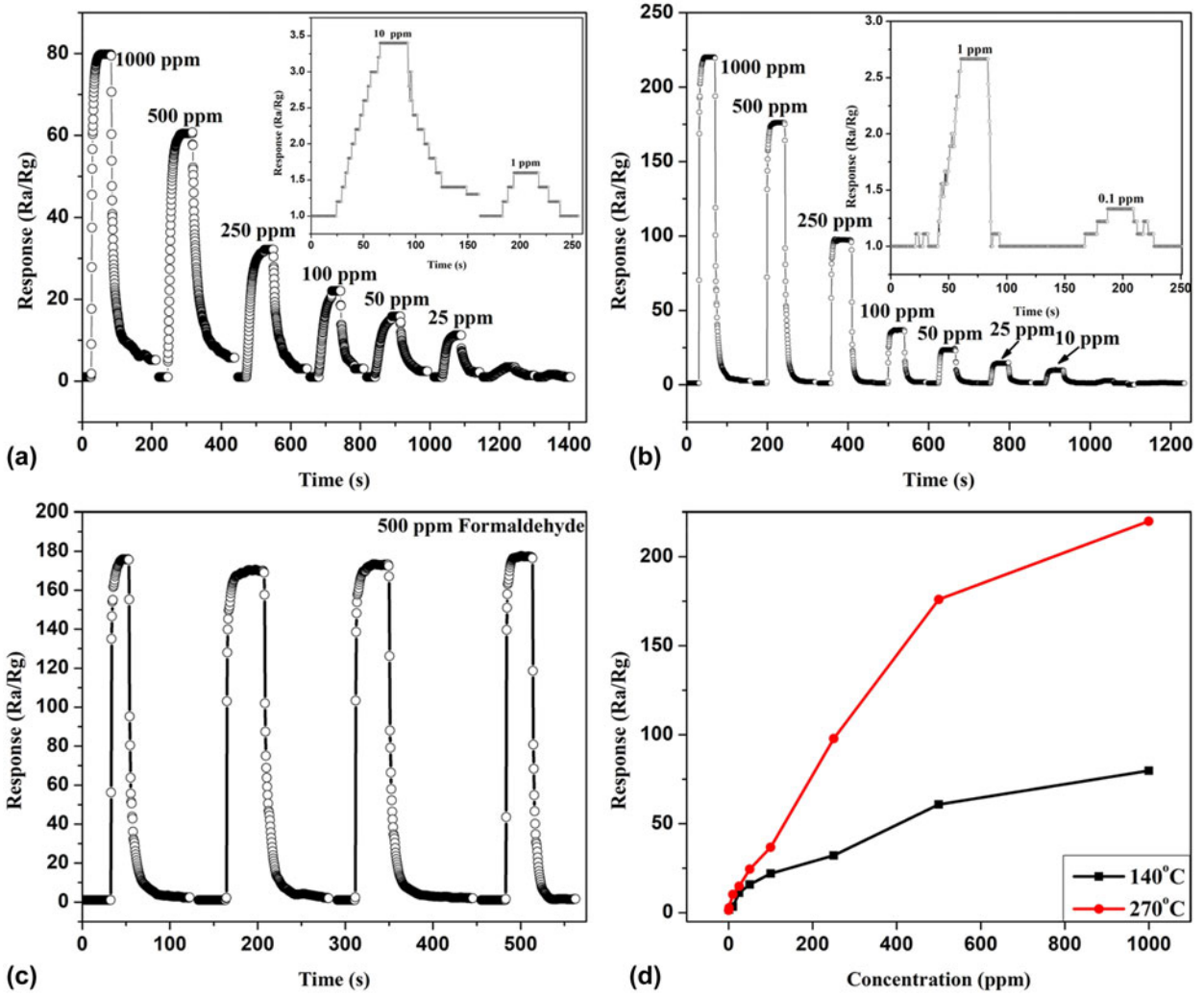


Figure 7: (a) Sensor response to various concentrations of formaldehyde at 140 °C, and (b) at 270 °C, (c) Repeatability of the sensor response at 270 °C, and (d) Sensor response versus concentration of formaldehyde at 140 and 270 °C.

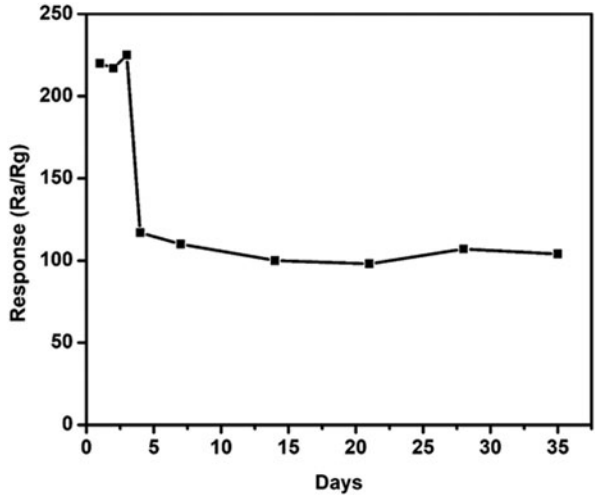


Figure 8: Stability of 4LBSO in responding to the presence of formaldehyde at 1000 ppm concentration.

$$HCHO(ad) + 2O^{2-}(ad) \rightarrow CO_2 + H_2O + 4e^- \quad . \quad (9)$$

This leads to a release of electrons that have been trapped by the adsorbed oxygen which in turn lowers the resistance of LBSO in accordance with our observation.

In order to understand the importance of this work with respect to previous reports on formaldehyde sensors, we have listed the main sensing parameters of this work and compared them with those of other reports in Table I.

Conclusion

BSO and LBSO microtubes, with varying concentrations of La^{3+} dopant, were synthesized successfully through electrospinning. Characterization by multiple analytical techniques revealed the formation of microtubes having a length of 2.5 μm and a diameter of 280 nm, made up of ~55 nm nanoparticles

https://doi.org/10.1557/jmr.2019.95 Published online by Cambridge University Press

© Materials Research Society 2019

TABLE I: A comparison of formaldehyde sensing properties of La-doped $BaSnO_3$ and similar metal oxide-based sensors.

Material	Operating temperature (°C)	Highest response (R_a/R_g)	Selectivity (S_1/S_2)	Detection limit (ppm)	Ref.
$Ga_{1.4}In_{0.6}O_3$ nanofibers loaded with 1 wt% IrO_2	280	44 at 200 ppm	Poor (2.93)	0.06	[51]
Potential barrier modulated In_2O_3 hierarchical structures	260	8.6 at 100 ppm	Poor (2.43)	1	[52]
Al-doped zinc oxide thin film	350	95.5 at 20 ppm	Good (6.57)	0.04	[53]
rGO/$ZnSnO_3$ with 3 wt% rGO	103	12.8 at 10 ppm	Good (5.12)	0.1	[54]
Mesoporous In_2O_3 nanoparticles synthesized by hydrothermal method	280	20 at 10 ppm	Poor (2.23)	10	[55]
$ZnSnO_3$ hierarchical microspheres decorated with NiO nanosheets	85	10.4 at 1 ppm	Good (4.16)	0.1 ppm	[56]
In_2O_3–SnO_2 with 3% In_2O_3	100	30.7 at 100 ppm	Good (3.07)	1	[57]
Cr_2O_3–ZnO hierarchical heterostructure	220	3.75 at 500 ppm	NA	5	[58]
CeO_2 polyhedral nanostructures	220	172 at 150 ppm	Poor (1.376)	1	[59]
Ag decorated SnO_2	125	14.4 at 10 ppm	Good (7.2)	0.53	[60]
SnO_2@rGO nanocomposite with 0.5% rGO	160	138 at 100 ppm	Good (3.89)	1	[61]
Modified SnO_2/Sn_3O_4 with Ag/Ag_2O	160	12.76 at 100 ppm	Good (4.8)	10	[62]
Layer by layer assembled In_2O_3/MoS_2	Room temperature	75.29% at 100 ppm	Poor (1.52)	0.2	[63]
La-doped $BaSnO_3$	270	220 at 1000 ppm	Good (6.29)	0.1	This work
La-doped $BaSnO_3$	140	80 at 1000 ppm	High (57.14)	1	This work

of LBSO. LBSO sample prepared with 4 wt% La^{3+} dopants showed the best response to formaldehyde vapor and at 270 °C, the sensor exhibited response as high as 220–1000 ppm concentration of formaldehyde. The response of the 4LBSO sensor decreased upon increasing and decreasing the temperature, and at 140 °C, it gave a response of 80. It was also noted that the detection limit of the sample was reduced to 0.1 ppm when operating at 270 °C with a response of 1.33, whereas the detection limit was 1 ppm when the sensor operated at 140 °C with a response of 1.6. The stability of 4LBSO reduced rapidly on the fourth day, following which the sample maintained its stability over a duration of 30 days, which signifies the potential of La^{3+}-doped $BaSnO_3$ for application as a stable formaldehyde sensor.

Materials and methods

Materials

Barium nitrate ($Ba(NO_3)_2$, 99.999%, Aladdin Chemicals, Ontario, California), tin(IV) chloride pentahydrate ($SnCl_4{\cdot}5H_2O$, 99.999%, Aladdin Chemicals), lanthanum nitrate hexahydrate ($La(NO_3)_3{\cdot}6H_2O$, 99.999%, Aladdin Chemicals), polyvinylpyrrolidone (PVP, $(C_6H_9NO)_n$, 99.999%, Aladdin Chemicals), and dimethylformamide (DMF, $HCON(CH_3)_2$, Aladdin Chemicals) were purchased and used without further purification.

Synthesis of undoped and La^{3+}-doped BSO microtubes

Firstly, a solution of $Ba(NO_3)_2$ and $SnCl_4{\cdot}5H_2O$ was prepared by dissolving in a mixture containing DMF and ethanol in the ratio of 1:9. The solution was stirred for 30 min followed by addition of 10% PVP by weight in the solution. The solution was then stirred for 6 h to form a homogeneous solution. The obtained solution was then transferred into a syringe with a conventional single nozzle. Electrospinning was carried out at an applied voltage of 15 kV while the collection distance was 30 cm. The microtubes were collected on an Al foil and dried at a temperature of 95 °C for 4 h. The sample was then annealed under an oxidative atmosphere in a controlled temperature regime (heating @ 1 °C/min from room temperature to 700 °C, maintaining at 700 °C for 6 h and cooling down to room temperature @ 1 °C/min) to improve the crystallinity of the samples.

To prepare doped BSO samples, $La(NO_3)_3{\cdot}6H_2O$ precursor was added in appropriate ratio along with the other precursors as above in the mixture of DMF and ethanol while keeping the rest of the procedure unchanged. The various samples thus prepared were named as BSO (undoped), 2LBSO (2 wt% La doped), 3LBSO (3 wt% La doped), 4LBSO (4 wt% La doped), 5LBSO (5 wt% La doped), and 6LBSO (6 wt% La doped).

Materials characterization

To understand the thermal behavior of the precursors thermogravimetric differential scanning calorimetry (TG-DSC), data were recorded in the temperature range of 25–1000 °C with a scan rate of 5 °C/min using a Netzsch STA449F3 system, Netzsch, Selb, Germany. Information on the crystallinity and phase composition of the samples was obtained by X-ray diffraction (XRD) analysis in a Bruker D8 diffractometer (Bruker, Billerica, Massachusetts) illuminated with Cu K_α radiation at a scan rate of 15°/min. The electron microscopic images of 4LBSO sample were obtained using a Hitachi S-4800 (Hitachi, Tokyo, Japan) Field Emission Scanning Electron Microscope (FESEM) at an accelerating voltage of 10 kV. The electronic band gap of the samples was compared by measuring the UV-Vis diffused absorption spectra in a Shimadzu UV-3600 spectrophotometer, Shimadzu, Kyoto, Japan. The elemental composition and oxidation states of the species present in the 4LBSO sample were analyzed by X-ray Photoelectron Spectroscopy (XPS) performed by a Thermo

https://doi.org/10.1557/jmr.2019.95 Published online by Cambridge University Press

© Materials Research Society 2019

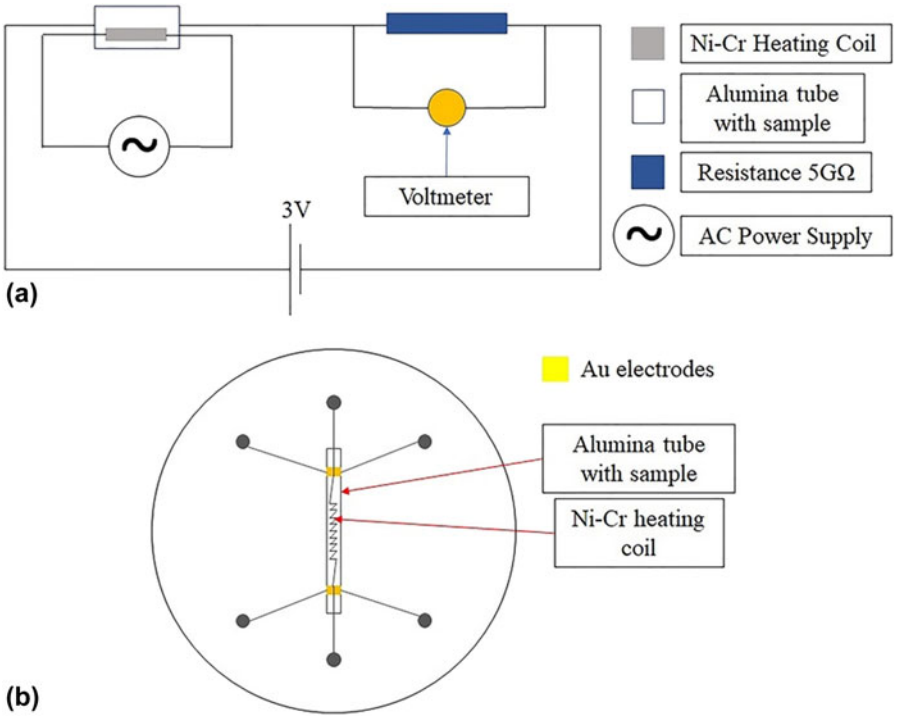


Figure 9: (a) Circuit used for gas sensing and (b) schematic diagram of a gas sensor.

ESCALAB 250 XI spectrometer, Thermo scientific, Waltham, Massachusetts. The specific surface area of 4LBSO was evaluated by Micrometrics ASAP 2020 apparatus, Micrometrics, Norcross (Atlanta), Georgia.

Fabrication of gas sensor and gas-sensing property measurement

Figure 9(a) shows the schematic circuit diagram of the gas sensing measurement set up used in this work. The LBSO-based formaldehyde sensor was made by coating the exterior surface of an alumina tube with a slurry of the as-prepared LBSO microtubes obtained by dispersing in terpineol followed by drying at 80 °C for 10 h, a step necessary to remove the terpineol. The alumina tube had two gold contacts at two ends to enable resistance measurement across the LBSO film when connected with a multimeter. A Ni–Cr coil was inserted through the alumina tube to heat the sensor at temperatures in the range of 20–450 °C [Fig. 9(b)]. Gas sensing measurement was carried out at a relative humidity of 50% in a sealed chamber.

Acknowledgments

This work was supported by NSFC (No. 61671019).

References

1. **Y. Zhang, L. Luo, C. Han, H. Lv, D. Chen, G. Shen, K. Wu, S. Pan, F. Ye, Y. Zhang, L. Luo, C. Han, H. Lv, D. Chen, G. Shen, K. Wu, S. Pan, and F. Ye**: Design, synthesis, and biological activity of tetrahydrobenzo[4,5]thieno[2,3-*d*]pyrimidine derivatives as anti-inflammatory agents. *Molecules* **22**, 1960 (2017).
2. **F. Zhang, G. Qu, E. Mohammadi, J. Mei, and Y. Diao**: Solution-processed nanoporous organic semiconductor thin films: Toward health and environmental monitoring of volatile markers. *Adv. Funct. Mater.* **27**, 1701117 (2017).
3. **X-Y. Xu and B. Yan**: Eu(III)-functionalized ZnO@MOF heterostructures: Integration of pre-concentration and efficient charge transfer for the fabrication of a ppb-level sensing platform for volatile aldehyde gases in vehicles. *J. Mater. Chem. A* **5**, 2215 (2017).
4. **Y. Zhang, J. Zhang, Q. Liu, Y. Zhang, J. Zhang, and Q. Liu**: Gas sensors based on molecular imprinting technology. *Sensors* **17**, 1567 (2017).
5. **G. Zilberstein, R. Zilberstein, S. Zilberstein, U. Maor, E. Baskin, S. Zhang, and P.G. Righetti**: A miniaturized sensor for detection of formaldehyde fumes. *Electrophoresis* **38**, 2168 (2017).
6. **X. Wang, H. Li, M. Ni, L. Wang, L. Liu, H. Wang, and X. Guo**: Excellent formaldehyde gas-sensing properties of ruptured Nd-doped In_2O_3 porous nanotubes. *J. Electron. Mater.* **46**, 363 (2017).
7. **H. Wang, Y. Chi, X. Gao, S. Lv, X. Chu, C. Wang, L. Zhou, and X. Yang**: Amperometric formaldehyde sensor based on a Pd nanocrystal modified C/Co_2P electrode. *J. Chem.* **2017**, 1 (2017).
8. **I. Pötzelberger, C.C. Mardare, L.M. Uiberlacker, S. Hild, A. I. Mardare, and A.W. Hassel**: Electrocatalysis on copper–palladium alloys for amperometric formaldehyde sensing. *RSC Adv.* **7**, 6031 (2017).

https://doi.org/10.1557/jmr.2019.95 Published online by Cambridge University Press

© Materials Research Society 2019

9. **N. Barsan, D. Koziej, and U. Weimar**: Metal oxide-based gas sensor research: How to? *Sens. Actuators, B* **121**, 18 (2007).
10. **A. Dey**: Semiconductor metal oxide gas sensors: A review. *Mater. Sci. Eng., B* **229**, 206 (2018).
11. **X. Chu, P. Dai, S. Liang, A. Bhattacharya, Y. Dong, and M. Epifani**: The acetone sensing properties of $ZnFe_2O_4$-graphene quantum dots (GQDs) nanocomposites at room temperature. *Phys. E* **106**, 326 (2018).
12. **X. Chu, J. Wang, L. Bai, Y. Dong, and W. Sun**: The gas sensing properties of $NiGa_2O_4$ nanofibers prepared by electrospinning method. *Mater. Sci. Eng., B* **228**, 45 (2018).
13. **X. Chu, J. Wang, L. Bai, Y. Dong, W. Sun, and W. Zhang**: Trimethylamine and ethanol sensing properties of $NiGa_2O_4$ nanomaterials prepared by co-precipitation method. *Sens. Actuators, B* **255**, 2058 (2018).
14. **P. Ranjan, P. Tiwary, A.K. Chakraborty, and R.M. Ajay**: Graphene oxide based free-standing films for humidity and hydrogen peroxide sensing. *J. Mater. Sci.: Mater. Electron.* **29**, 15946 (2018).
15. **S.G. Chatterjee, S. Samanta, D. Dey, S. Chatterjee, S. Santra, P. K. Guha, and A.K. Chakraborty**: Near room temperature sensing of nitric oxide using SnO_2/Ni-decorated natural cellulosic graphene nanohybrid film. *J. Mater. Sci.: Mater. Electron.* **29**, 20162 (2018).
16. **S. Gupta Chatterjee, S. Chatterjee, A.K. Ray, and A. K. Chakraborty**: Graphene–metal oxide nanohybrids for toxic gas sensor: A review. *Sens. Actuators, B* **221**, 1170 (2015).
17. **P. Tiwary, R. Mahapatra, and A.K. Chakraborty**: ZnO nanobristles prepared by one-step thermal decomposition of zinc nitrate as ultra-high response ethanol sensor at room temperature. *J. Mater. Sci.: Mater. Electron.*, 1 (2019).
18. **I. Chakraborty, N. Chakrabarty, A. Senapati, and A. K. Chakraborty**: CuO@NiO/Polyaniline/MWCNT nanocomposite as high-performance electrode for supercapacitor. *J. Phys. Chem. C* **122**, 27180 (2018).
19. **V. Augustyn**: Tuning the interlayer of transition metal oxides for electrochemical energy storage. *J. Mater. Res.* **32**, 2 (2017).
20. **G. Wang, X. Leng, S. Han, Y. Shao, S. Wei, Y. Liu, J. Lian, and Q. Jiang**: How to improve the stability and rate performance of lithium-ion batteries with transition metal oxide anodes. *J. Mater. Res.* **32**, 16 (2017).
21. **A.J. Pearson**: Structure formation and evolution in semiconductor films for perovskite and organic photovoltaics. *J. Mater. Res.* **32**, 1798 (2017).
22. **B. Ostrick, M. Fleischer, U. Lampe, and H. Meixner**: Preparation of stoichiometric barium stannate thin films: Hall measurements and gas sensitivities. *Sens. Actuators, B* **44**, 601 (1997).
23. **U. Lampe, J. Gerblinger, and H. Meixner**: Nitrogen oxide sensors based on thin films of $BaSnO_3$. *Sens. Actuators, B* **26**, 97 (1995).
24. **U. Lampe, J. Gerblinger, and H. Meixner**: Carbon-monoxide sensors based on thin films of $BaSnO_3$. *Sens. Actuators, B* **25**, 657 (1995).
25. **C.V.G. Reddy, S.V. Manorama, V.J. Rao, A. Lobo, and S. K. Kulkarni**: Noble metal additive modulation of gas sensitivity of $BaSnO_3$, explained by a work function based model. *Thin Solid Films* **348**, 261 (1999).
26. **W.Z. Lu, S.L. Jiang, D.X. Zhou, and S.P. Gong**: Structural and electrical properties of $Ba(Sn,Sb)O_3$ electroceramics materials. *Sens. Actuators, A* **80**, 35 (2000).
27. **S. Tao, F. Gao, X. Liu, and O.T. Sørensen**: Ethanol-sensing characteristics of barium stannate prepared by chemical precipitation. *Sens. Actuators, B* **71**, 223 (2000).
28. **Y.H. Ochoa, F. Schipani, C.M. Aldao, J.E. Rodríguez-Páez, and M.A. Ponce**: Modification of sensitivity of $BaSnO_3$ sensor due to parameters of synthesis and formation of the device. *J. Mater. Res.* **30**, 3423 (2015).
29. **W. Zhang, J. Tang, and J. Ye**: Structural, photocatalytic, and photophysical properties of perovskite $MSnO_3$ (M = Ca, Sr, and Ba) photocatalysts. *J. Mater. Res.* **22**, 1859 (2007).
30. **M.T. Buscaglia, M. Leoni, M. Viviani, and V. Buscaglia**: Synthesis and characterization of $BaSn(OH)_6$ and $BaSnO_3$ acicular particles. *J. Mater. Res.* **18**, 560 (2003).
31. **H. Karakas**: Electrospinning of nanofibers and their applications. *MDT "Electrospinning"* **3**, 1 (2014).
32. **J.V. Patil, S.S. Mali, A.S. Kamble, C.K. Hong, J.H. Kim, and P. S. Patil**: Electrospinning: A versatile technique for making of 1D growth of nanostructured nanofibers and its applications: An experimental approach. *Appl. Surf. Sci.* **423**, 641 (2017).
33. **N. Bhardwaj and S.C. Kundu**: Electrospinning: A fascinating fiber fabrication technique. *Biotechnol. Adv.* **28**, 325 (2010).
34. **B. Kannan, H. Cha, and I.C. Hosie**: *Nano-Size Polym* (Springer International Publishing, Cham, 2016); p. 309.
35. **Z-M. Huang, Y-Z. Zhang, M. Kotaki, and S. Ramakrishna**: A review on polymer nanofibers by electrospinning and their applications in nanocomposites. *Compos. Sci. Technol.* **63**, 2223 (2003).
36. **N. Chakrabarty and A.K. Chakraborty**: Controlling the electrochemical performance of β-$Ni(OH)_2$/carbon nanotube hybrid electrodes for supercapacitor applications by La doping: A systematic investigation. *Electrochim. Acta* **297**, 173 (2019).
37. **Y.H. Ochoa Muñoz, M. Ponce, and J.E. Rodríguez Páez**: Comparative study of two wet chemical methods of $BaSnO_3$ synthesis: Mechanism of formation of mixed oxide. *Powder Technol.* **279**, 86 (2015).
38. **W. Lu and H. Schmidt**: Lyothermal synthesis of nanocrystalline $BaSnO_3$ powders. *Ceram. Int.* **34**, 645 (2008).
39. **X. Chu**: Dilute CH_3SH-sensing characteristics of $BaSnO_3$ thick film sensor. *Mater. Sci. Eng., B* **106**, 305 (2004).
40. **S.M.D. Watson, K.S. Coleman, and A.K. Chakraborty**: A new route to the production and nanoscale patterning of highly smooth, ultrathin zirconium oxide films. *ACS Nano* **2**, 643 (2008).
41. **Y.V. Butenko, S. Krishnamurthy, A.K. Chakraborty, V. L. Kuznetsov, V.R. Dhanak, M.R.C. Hunt, and L. Šiller**:

https://doi.org/10.1557/jmr.2019.95 Published online by Cambridge University Press

© Materials Research Society 2019

Photoemission study of onionlike carbons produced by annealing nanodiamonds. *Phys. Rev. B* **71**, 075420 (2005).

42. **T.P. Nguyen, J. Ip, P. Jolinat, and P. Destruel**: XPS and sputtering study of the Alq_3/electrode interfaces in organic light emitting diodes. *Appl. Surf. Sci.* **172**, 75 (2001).
43. **L. Gao, F. Ren, Z. Cheng, Y. Zhang, Q. Xiang, and J. Xu**: Porous corundum-type In_2O_3 nanoflowers: Controllable synthesis, enhanced ethanol-sensing properties and response mechanism. *CrystEngComm* **17**, 3268 (2015).
44. **C. Wang, X. Cui, J. Liu, X. Zhou, X. Cheng, P. Sun, X. Hu, X. Li, J. Zheng, and G. Lu**: Design of superior ethanol gas sensor based on Al-doped NiO nanorod-flowers. *ACS Sens.* **1**, 131 (2016).
45. **M.F. Sunding, K. Hadidi, S. Diplas, O.M. Løvvik, T.E. Norby, and A.E. Gunnæs**: XPS characterisation of in situ treated lanthanum oxide and hydroxide using tailored charge referencing and peak fitting procedures. *J. Electron Spectrosc. Relat. Phenom.* **184**, 399 (2011).
46. **Y.X. Li, Z. Guo, Y. Su, X.B. Jin, X.H. Tang, J.R. Huang, X. J. Huang, M.Q. Li, and J.H. Liu**: Hierarchical morphology-dependent gas-sensing performances of three-dimensional SnO_2 Nanostructures. *ACS Sens.* **2**, 102 (2017).
47. **Y. Zhang, J. Zhang, J. Zhao, Z. Zhu, and Q. Liu**: Ag–$LaFeO_3$ fibers, spheres, and cages for ultrasensitive detection of formaldehyde at low operating temperatures. *Phys. Chem. Chem. Phys.* **19**, 6973 (2017).
48. **R.K. Mishra, G. Murali, T-H. Kim, J.H. Kim, Y.J. Lim, B-S. Kim, P.P. Sahay, and S.H. Lee**: Nanocube In_2O_3@RGO heterostructure based gas sensor for acetone and formaldehyde detection. *RSC Adv.* **7**, 38714 (2017).
49. **Z-W. Chen, Y-Y. Hong, Z-D. Lin, L-M. Liu, and X-W. Zhang**: Enhanced formaldehyde gas sensing properties of ZnO nanosheets modified with graphene. *Electron. Mater. Lett.* **13**, 270 (2017).
50. **X.H. Wu, Y. De Wang, H.L. Liu, Y.F. Li, and Z.L. Zhou**: Preparation and gas-sensing properties of perovskite-type $MSnO_3$ (M = Zn, Cd, Ni). *Mater. Lett.* **56**, 732 (2002).
51. **Q. Gao, S. Ao, H. Chen, X. Zou, C. Wei, and G-D. Li**: Enhanced formaldehyde sensing properties of IrO_2-loaded porous foam-like $Ga_{1.4}In_{0.6}O_3$ nanofibers with ultrathin pore walls. *J. Alloys Compd.* **732**, 856 (2018).
52. **S. Wang, J. Cao, W. Cui, L. Fan, X. Li, and D. Li**: Oxygen vacancies and grain boundaries potential barriers modulation facilitated formaldehyde gas sensing performances for In_2O_3 hierarchical architectures. *Sens. Actuators, B Chem.* **255**, 159 (2018).
53. **C-Y. Chi, H-I. Chen, W-C. Chen, C-H. Chang, and W-C. Liu**: Formaldehyde sensing characteristics of an aluminum-doped zinc oxide (AZO) thin-film-based sensor. *Sens. Actuators, B Chem.* **255**, 3017 (2018).
54. **J. Sun, S. Bai, Y. Tian, Y. Zhao, N. Han, R. Luo, D. Li, and A. Chen**: Hybridization of $ZnSnO_3$ and rGO for improvement of formaldehyde sensing properties. *Sens. Actuators, B Chem.* **257**, 29 (2018).
55. **S. Zhang, P. Song, Z. Yang, and Q. Wang**: Facile hydrothermal synthesis of mesoporous In_2O_3 nanoparticles with superior formaldehyde-sensing properties. *Phys. E* **97**, 38 (2018).
56. **S. Bai, Y. Tian, Y. Zhao, H. Fu, P. Tang, R. Luo, D. Li, A. Chen, and C.C. Liu**: Construction of NiO@$ZnSnO_3$ hierarchical microspheres decorated with NiO nanosheets for formaldehyde sensing. *Sens. Actuators, B* **259**, 908 (2018).
57. **W. Ge, Y. Chang, V. Natarajan, Z. Feng, J. Zhan, and X. Ma**: In_2O_3–SnO_2 hybrid porous nanostructures delivering enhanced formaldehyde sensing performance. *J. Alloys Compd.* **746**, 36 (2018).
58. **T. Wang, B. Liu, Q. Li, and S. Wang**: Controllable construction of Cr_2O_3–ZnO hierarchical heterostructures and their formaldehyde gas sensing properties. *Mater. Lett.* **221**, 260 (2018).
59. **S. Hussain, N. Aslam, X. Yang, M. S. Javeed, Z. Xu, M. Wang, G. Liu, and G. Qiao**: Unique polyhedron CeO_2 nanostructures for superior formaldehyde gas-sensing performances. *Ceram. Int.* **44** (16), 19624 (2018).
60. **D. Liu, J. Pan, J. Tang, W. Liu, S. Bai, and R. Luo**: Ag decorated SnO_2 nanoparticles to enhance formaldehyde sensing properties. *J. Phys. Chem. Solids* **124**, 36 (2018).
61. **X. Rong, D. Chen, G. Qu, T. Li, R. Zhang, and J. Sun**: Effects of graphene on the microstructures of SnO_2@rGO nanocomposites and their formaldehyde-sensing performance. *Sens. Actuators, B Chem.* **269**, 223 (2018).
62. **H. Yu, J. Li, Y. Tian, and Z. Li**: Environmentally friendly recycling of SnO_2/Sn_3O_4 from tin anode slime for application in formaldehyde sensing material by Ag/Ag_2O modification. *J. Alloys Compd.* **765**, 624 (2018).
63. **D. Zhang, C. Jiang, and J. Wu**: Layer-by-layer assembled In_2O_3 nanocubes/flower-like MoS_2 nanofilm for room temperature formaldehyde sensing. *Sens. Actuators, B Chem.* **273**, 176 (2018).

https://doi.org/10.1557/jmr.2019.95 Published online by Cambridge University Press

© Materials Research Society 2019